USING BOTH MINOR AND MAJOR ARC DATA FOR GLOBAL SURFACE WAVE DIFFRACTION TOMOGRAPHY

Anatoli L. Levshin[a,1], Michael P. Barmin[a], Michael H. Ritzwoller[a], and Jeannot Trampert[b]

[a]Center for Imaging the Earth's Interior, Department of Physics, University of Colorado at Boulder, Campus Box 390, Boulder, CO 80309, USA.
[b]Department of Geophysics, University of Utrecht, P.O. Box 80021 3508 TA Utrecht, The Netherlands.

Abstract

We extend a previously developed technique of global surface wave diffraction tomography to accommodate major arc data. The addition of major arc data provides better spatial and azimuthal resolution for regions with relatively poor coverage by minor arc paths. Examples of Rayleigh wave phase velocity tomography at 50 and 100 s are presented. We show that major arc data, which have a higher level of noise, nonetheless provide important additional information about phase velocity distribution, especially for the Southern Hemisphere.

1. Introduction

This paper presents a further development of the tomographic techniques to invert surface wave dispersion measurements to two-dimensional maps of phase or group velocities for a set of periods. In the paper by Barmin et al. (2001), we described a method of surface

---

[1]Corresponding author

E-mail address: levshin@ciei.colorado.edu

wave tomography based on geometrical ray-theory and largely *ad hoc* Gaussian smoothing constraints. This method, which will be addressed here as Gaussian tomography, was used in numerous studies of the regional Earth's structure (Levshin et al., 2001; Ritzwoller et al., 2001). However, the ray-theory is essentially a high frequency approximation, and it is not justified in the presence of heterogeneities whose length-scale is comparable to the wavelength of the wave [e.g., Woodhouse (1974), Wang & Dahlen (1995)]. For ray approximation to be valid, the first Fresnel zone must be smaller than the scale-length of the heterogeneity. This means that the lateral resolution of seismic models based on ray-theory is significantly limited.

The use of Born/Rytov's approximation for surface wave scattering (e.g., Woodhouse & Girnius, 1982; Yomogida & Aki, 1987; Snieder & Romanowicz, 1988; Bostock & Kennett, 1992; Friederich et al., 1993, Friederich 1999; Meier et al., 1997; Spetzler et al., 2001, 2002; Yoshizawa & Kennett, 2002; Snieder, 2002) has provided a theoretical framework for introducing a new technique for surface wave tomography which takes into account the finite width of the sensitivity zone around the great circle surface wave path (Ritzwoller et al., 2002). The sensitivity zone corresponds approximately to the first Fresnel zone. Its maximum width increases with the epicentral distance and wavelength. This approach, which we call diffraction tomography, was applied for global surface wave tomography and was also used to construct a 3D global shear velocity model of the crust and upper mantle (Shapiro & Ritzwoller, 2002). However, this approach was designed to use only minor arc data. Some regions of the Earth, especially in the Southern hemisphere, cannot be effectively covered by minor arc paths due to the sparse network of seismic stations. The use of major arc data in tomographic inversions may significantly improve the spatial resolution of the tomographic maps and azimuthal coverage, which is important for studies of azimuthal anisotropy (Trampert & Woodhouse, 2003). Minor and major arc observations have been previously used in tomographic studies only in the great circle approximation (Trampert & Woodhouse, 1995, 1996, 2003; Ekström et al., 1997). In this paper we extend diffraction tomography to accommodate data from both arcs. To do this, we define the zone of sensitivity for a major arc path using the Born/Rytov's approximation. Due to the focusing effects at antipodes of

the source and the receiver, the form of this zone is more complicated than in the case of a minor arc. We apply this approach to surface wave phase velocity measurements obtained by Trampert & Woodhouse (1995) and estimate the improvements in spatial resolution and the reliability of tomographic maps. We pay special attention to the Southern hemisphere, and, particularly, the regions of the Southern Pacific and Antarctica for which the coverage by minor arc paths is still much worse than for the Northern hemisphere.

2. Fresnel Zones and Sensitivity Kernels for Major Arc Paths

The rule by which we define the sensitivity zone for a given surface wave is quite simple. Any point O on the surface of the globe which satisfies the inequality

$$|\Delta_{S-O} + \Delta_{O-R} - \Delta_{S-R}| \leq \lambda(T)/N \tag{1}$$

belongs to this zone. Here Δ_{S-O} and Δ_{O-R} are the epicentral distances from epicenter to the point O and from point O to the receiver (or vice versa). Δ_{S-R} is the distance from the source to the receiver along a minor/major arc depending on which kind of data is considered (all distances are in km). $\lambda(T)$ is the wavelength for a given period T, and N is a constant. We use $N = 8/3$ recommended by Spetzler et al. (2001, 2002). Figure 1 (top) shows schematically how such a zone is defined on a tomographic grid. The zones of sensitivity are shown in Figure 2 for minor and major arcs for 50 s and 100 s Rayleigh waves for the PREM model of the Earth (Dziewonski & Anderson, 1981) at different epicentral distances.

We calculate the traveltime of surface waves from the source to the receiver as an integral over the Earth's surface S:

$$t_q^{\text{diff}}(T) = \int_S K_q(\mathbf{r}, T) v_q^{-1}(\mathbf{r}, T) dS \tag{2}$$

where K_q is the sensitivity kernel, and the vector $\mathbf{r}$ is a position vector on the Earth's surface. Similar to Vasco et al. (1995) we assume that for a given epicentral distance the value of K_q inside the sensitivity zone is constant and is inversely proportional to the width of the zone. In the case, when this width is less than $\lambda/4$, the sensitivity is truncated to the value at the

3

zero epicentral distance to avoid nonphysically large amplitude in the kernel. The sensitivity kernel is zero outside the sensitivity zone and is normalized by the condition

$$\int_S K_q(\mathbf{r}, T) dS = 1. \tag{3}$$

An example of the sensitivity kernel K_q as a function of an epicentral distance is shown in Figure 1 (middle) and as a function of the distance from the great circle connecting source and receiver in Figure 1 (bottom, the dashed line). Thisapproximation is compared with Born/Rytov approximation (bottom, solid line).

Extending the definition of the sensitivity zone and kernels for major arc data allows us to combine minor and major arc data for tomographic inversion of existing phase velocity measurements.

3. Tomographic Inversion

0.0.1 Inversion technique

For tomographic inversion of the combination of minor and major arc data, we use the method described in Barmin et al., (2001). This method is based on minimizing the following objective function for an isotropic map $\mathbf{m}$ consisting of velocity perturbations relative to a reference map:

$$(\mathbf{Gm} - \mathbf{d})^T \mathbf{C}^{-1} (\mathbf{Gm} - \mathbf{d}) + \alpha^2 ||F(\mathbf{m})||^2 + \beta^2 ||H(\mathbf{m})||^2. \tag{4}$$

Equation (4) is a linear combination of data misfit, model roughness, and the amplitude of the perturbation to the reference map. $\mathbf{G}$ is the forward operator that computes traveltime from a map using equation (2). $\mathbf{d}$ is the data vector whose components are the observed traveltime residuals relative to the reference map. $\mathbf{C}$ is the data covariance matrix or matrix of data weights. F is a Gaussian spatial smoothing operator, and H is an operator that penalizes the norm of the model in regions of poor path coverage. We note here that the spatial smoothing operator is defined over a 2D tomographic map as follows

$$F(\mathbf{m}) = \mathbf{m}(\mathbf{r}) - \int_S S(\mathbf{r}, \mathbf{r}') \mathbf{m}(\mathbf{r}') d\mathbf{r}' , \tag{5}$$

4

where S is a smoothing kernel:

$$S(\mathbf{r}, \mathbf{r}') = K_0 \exp\left(-\frac{|\mathbf{r} - \mathbf{r}'|^2}{2\sigma^2}\right) \tag{6}$$

$$\int_S S(\mathbf{r}, \mathbf{r}')d\mathbf{r}' = 1, \tag{7}$$

and σ is the spatial smoothing width or correlation length. The vector $\mathbf{r}$ is a position vector on the earth's surface. Values at spatial points between nodes are computed with bilinear interpolation. The choice of the damping coefficients α and β and the smoothing width σ is *ad hoc*. We typically apply spatial smoothing widths from 150 to 300 km.

As described in detail in Barmin et al. (2001), both the forward and inverse problems stated above are solved on a grid. For global tomography, we usually use the $2° \times 2°$ equatorial grid.

0.0.2 Path density

The improvement in coverage of the Earth by surface wave paths with an addition of major arc data may be presented in terms of path density. In the case of Gaussian Tomography, we defined path density $\rho(\mathbf{r})$ as the number of paths intersecting a square cell of the fixed area with center at the point $\mathbf{r}$. For diffraction tomography, this definition makes no sense, because each path now is not a linear object but an area object. For this reason, we introduce a pseudo path density $\rho_D(\mathbf{r}, T)$ by means of the formula

$$\rho_D(\mathbf{r}, T) = \sum_q K_q(\mathbf{r}, T)\Delta_q \tag{8}$$

where Δ_q is the distance between source and receiver along a minor or major arc for the q-th path, and K_q is the sensitivity kernel from equation (2). Summation is made for all paths for which the point $\mathbf{r}$ is inside the sensitivity zone. This formulation approximates path density in the limit when Fresnel zone becomes very narrow.

0.0.3 Resolution analysis

The solution of (4) describing an isotropic map of velocity perturbations is

$$\hat{\mathbf{m}} \;=\; \mathbf{G}^T \mathbf{C}^{-1} \delta \mathbf{t} = \left(\mathbf{G}^T \mathbf{C}^{-1} \mathbf{G} \right) \mathbf{m} = \mathcal{R} \mathbf{m} \qquad (9)$$

where matrix $\mathcal{R}$

$$\mathcal{R} \;=\; \left(\mathbf{G}^T \mathbf{C}^{-1} \mathbf{G} + \mathbf{Q} \right)^{-1} \mathbf{G}^T \mathbf{C}^{-1} \mathbf{G}. \qquad (10)$$

is the resolution matrix. In this application, each row of $\mathcal{R}$ is a resolution map defining the resolution at one spatial node. The resolution matrix is consequently very large and the information it contains is somewhat difficult to utilize. We attempt to summarize the information in each resolution map by estimating a scalar quantity, which we call the spatial resolution at each point of the grid. The spatial resolution of tomographic maps is determined here in a slightly different manner than in Barmin et al. (2001). To estimate spatial resolution, we fit a cone to each resolution map. This cone approximates the response of the tomographic procedure to a δ-like perturbation at the target node. The radius of the cone base was taken in Barmin et al. (2001) as the value of the spatial resolution. It was observed that in many cases the shape of response resembles a Gaussian bell, and therefore the old estimate was biased to larger values of the spatial resolution. To eliminate this bias, we introduce a new estimate of the spatial resolution as a γ parameter describing a Gaussian bell function

$$A \exp \left(-\frac{|\mathbf{r}|^2}{2\gamma^2} \right) \qquad (11)$$

which is the best fit to a given resolution map. Here A is an amplitude at the target node. The Gaussian function is defined on the base of the fitting cone enlarged by factor k. To construct the optimal Gaussian bell, we convert negative values of the map to positive ones, and discard as random noise all points of the map with amplitude less than A/m. We use *ad hoc* values $k = 1.2$ and $m = 10$.

4. Data

0.0.4 Input data and data handling

Surface wave phase velocity measurements described by Trampert & Woodhouse (1995) were used in the tomographic inversion. We limited ourselves to two periods, 50 s and 100 s, and analyzed only Rayleigh wave data for these periods. In what follows, we will refer to minor arc Rayleigh wave observations as R1 and to major arc observations of the same waves as R2. The number of paths for the initial data set (R1, R2) is given in Table 1 (column 3). To find possible outliers, we apply the two-stage procedure. At the first stage, we trace all paths contained in raw data across maps predicted by the current global 3D model of Shapiro & Ritzwoller (2002). Ray-tracing is done using the same algorithm as in tomographic inversion. Figure 3 shows the relative traveltime residuals [(observed - predicted)/predicted] for the raw data as a function of distance are shown in Figure 3. The mean values and $\pm 2.5 \times rms$ in the window sliding along the epicentral distance are presented as well. The gaps in data at the epicentral distances $\Delta \approx 160° - 200°$ and $340° - 360°$ are due to interference of minor and major arc wave trains near the epicenter and its antipode, which makes phase measurements in these ranges unreliable. A significant number of outliers in data is evident. Data rejection is based on statistics of phase velocity residuals, which are approximately proportional to the relative traveltime residuals. Corresponding average values of rms for phase velocity residuals are given in the Table 1 (column 4). Only paths with relative residuals between $\pm 2.5 \times rms$ are selected for further analysis. The numbers of selected paths are presented in Table 1 (column 5).

At the second stage, we apply to these selected paths a consistency test (Ritzwoller & Levshin, 1998). We check measurements along close paths with end points inside the same cells of the size $110 km \times 110 km$. We delete duplicates and reject inconsistent measurements. After this test, the numbers of selected paths are reduced drastically as can be seen from Table 1. This procedure allows us also to estimate the inherent errors of measurements. Average rms values for the whole set of close paths with consistent travel times are given in the column 6 of Table 1.

The absolute phase traveltime residuals for data left after this two-stage cleaning grow with distance. The *rms* values of these residuals for 50 and 100 s Rayleigh waves are shown in Figure 4 (top). These values are more-less monotonically increase with epicentral distance, except the range between $\Delta = 125°$ and $\Delta = 225°$ where we observe a significant growth of *rms*. This may indicate the problems with accurate measurements of phase velocities caused by the interference of R1 and R2 waves. By this reason we discard the measurements at this interval. The general increase of phase traveltime residuals with distance may be partly due to the systematic decrease of signal-to-noise ratio. One possible way to reduce the effect of noise is to introduce weighting of data in the inversion procedure. The weights $W(\Delta)$ we use are inversely proportional to the smoothed function approximating the dependence of the square root of the traveltime *rms* on epicentral distance (Figure 4, bottom).

0.0.5   Path density

The Pacific Ocean and Antarctic regions are relatively poorly covered by minor arc observations due to rare network of stations. For these regions adding major arc observations to the tomographic input is especially important. The left side of Figure 5 shows the density of 50 s Rayleigh and Love wave paths across Eurasia and surroundings, the Pacific Ocean, and Antarctica when only data from minor arcs are used. The right side of the same figure demonstrates the additional density provided for the same regions by data from major arcs. Evidently, data from major arcs significantly improves coverage for the Southern Pacific, Antarctica, Africa, and the Indian Ocean. Path densities for 100 s surface waves have a very similar pattern.

0.0.6   Spatial resolution

In Figure 6, we show maps of the spatial resolution obtained with minor arc data only and with a combination of minor and major arc data for 50 s surface waves crossing Eurasia, the Pacific, and Antarctica. We see significant improvement in resolution across the last two

regions when both types of data are used. The similar pattern is obtained for 100 s surface waves.

5. Results of Tomographic Inversion

Results of the tomographic inversion of combined minor and major arc data [R1+R2] for Rayleigh waves at periods 50 and 100 s are shown in the left sides of Figures 7 and 8. The right side presents the results of tomography when only R1 data are analyzed. The same set of parameters was used in both inversions. Three different sets of maps are shown covering Eurasia and surroundings, the Pacific, and Antarctica. Differential maps [(R1+R2) - R1] (Figure 9) for the same regions demonstrate changes in phase velocities, which result from the addition of major arc data. These changes are relatively small (in the range of ±0.25 km/s, or 6 %), but still essential, especially for the Southern Pacific and Antarctica. The effect of including major arc data in the tomographic data set can also be demonstrated by comparison of changes in tomographic maps for two regions of the same size: the northern part of the Northern Hemisphere for latitudes $45°N - 90°N$ and the southern part of the Southern Hemisphere for latitudes $45°S - 90°S$. The first region is well covered by R1 paths, and the second region is relatively poorly covered. Table 2 shows the correlation between maps $[R1 + R2]$, R1 for 50 and 100 s for these two regions. It is evident that for the Northern Hemisphere changes in maps are significantly smaller than for the Southern Hemisphere. The correlation between two sets of maps is stronger, and the *rms* of the absolute difference between the two maps is almost two times smaller for the North.

The question arises, does the addition of major arc data improve the maps providing more accurate and more detailed information on phase velocity distribution across the globe, or does it increase the noise in the obtained images? One of the ways to answer this question is to examine the difference between the fit of minor arc data to maps obtained with these data and to maps obtained with data from both arcs. Table 3 contains the information about misfit between observed and predicted traveltimes and group velocities for different combinations of Rayleigh wave maps and data sets for path covering the whole Earth. One

can see that addition of major arc data only slightly decreases the fit of observations from R1 data to the prediction. Variance reduction relative to the reference model for R1 paths traced across the [R1+R2] maps is of the order of 10% and is ~ 1.5 times less than with [R1] maps. This could be explained by predominance of R1 data on R2 data. To evaluate if this conclusion is valid also for data related only to the Southern Hemisphere where number of R1 paths is relatively small, we selected R1 paths which are completely inside the Southern Hemisphere. Corresponding data fits are shown in Table 4. It is clear that even in this case the misfits between minor arc data and the prediction from [R1+R2] maps and [R1] maps are quite close. In general, the misfit between R2 data and the prediction from the R1 maps is noticeably higher than for the R1 data, The misfit significantly decreases when R2 data are used in inversion. All this indicates that the addition of R2 data does not decrease the quality of tomographic images.

6. Discussion and Conclusions

In the described approach, we solve a practical problem of inversion of numerous surface wave dispersion measurements along minor and major arcs into reliable tomographic maps of the surface wave velocities for given set of periods on the Earth's surface. Our tomographic technique is based on several approximations:

(1) We accept the basic ideas of the Born/Rytov theory, an asymptotic theory for forward scattering in the case when local inhomogeneities are much less than wavelengths. In reality there is a wide spectrum of inhomogeneities (Chevrot et al., 1998), and the lower part of the inhomogeneity spectrum does not comply with this constraint.

(2) We neglect path wander (Ritzwoller et al., 2002; Yoshizawa & Kennett, 2002), considering these effects at periods $T \geq 50s$ as secondary in comparison with scattering effects.

(3) We simplify the expression for the sensitivity kernel in comparison with the one obtained from the Born/Rytov theory (Spetzler et al., 2002). This approximation describes quite well the main effects of forward scattering.

We applied this tomographic technique to the phase velocity data set obtained by Trampert & Woodhouse (1995). The analysis of the major arc measurements indicates that they are more noisy than the minor arc data and need to be weighted out. Nevertheless, our tomographic simulations show that combining minor and major arc data in the frame of the diffraction tomography may significantly improve the spatial (and azimuthal) resolution of data without degrading the data fit to predicted models of each type of observation. This is especially true for the Southern hemisphere where the existing seismic network is sparse.

Acknowledgements

References

Barmin, M.P., A.L. Levshin, and M.H. Ritzwoller, 2001. A fast and reliable method for surface wave tomography, Pure Appl. Geophys., 158: 1351-1375.

Bostock, M.G. and B.L.N. Kennett, 1992. Multiple scattering of surface waves from discrete obstacles, Geophys. J. Int., 108: 52-70.

Chevrot, S., J.P. Montagner, and R. Snieder, 1998. The spectrum of tomographic earth models, Geophys. J. Int., 133: 783-788.

Dziewonski, A. M. and D. L. Anderson, 1981. Preliminary Reference Earth Model, Phys. Earth. Planet. Int., 25: 297-356.

Ekström, G., J. Tromp, and E.W.F. Larson, 1997. Measurements and global models of surface wave propagation, J. Geophys. Res.: 102, 8147 - 8158.

Friederich, W., E. Wielandt, and S. Strange, 1993. Multiple forward scattering of surface waves; Comparison with an exact solution and the Born single-scattering methods, Geophys. J. Int., 112: 264-275.

Friederich, W., 1999. Propagation of seismic shear and surface waves in a laterally heterogeneous mantle by multiple forward scattering, Geophys. J. Int., 136: 180-204.

Levshin, A.L., M.H. Ritzwoller, M.P. Barmin, A. Villaseñor, 2001. New constraints on the Arctic crust and uppermost mantle: Surface wave group velocities, P_n, and S_n, Phys. Earth. Planet. Int. 123: 185-204.

Meier, T., S. Lebedev, G. Nolet, and F.A. Dahlen, 1997. Diffraction tomography using multimode surface waves, J. Geoph. Res., 102(B4): 8255-8267.

Ritzwoller, M.H. and A.L. Levshin, 1998. Eurasian surface wave tomography: Group velocities, J. Geoph. Res., 103: 4839-4878.

Ritzwoller, M.H., N.M. Shapiro, A.L. Levshin, and G.M. Leahy, 2001. Crustal and upper mantle structure beneath Antarctica and surrounding oceans, J. Geoph. Res., 106(B12): 30,645-30,670.

Ritzwoller, M.H., N.M. Shapiro, M.P. Barmin, and A.L. Levshin, 2002. Global surface wave diffraction tomography, J. Geoph. Res., 107 : B12, 2335,doi:10.1029/2002JB001777.

Shapiro, N.M. and M.H. Ritzwoller, 2002. Monte Carlo inversion for a global shear velocity model of the crust and upper mantle, Geophys. J. Int., 151: 88-105.

Snieder, R. and B. Romanowicz, 1988. A new formalism for the effect of lateral heterogeneity on normal modes and surface waves – I: Isotropic perturbations, perturbations of interfaces and gravitational perturbations, Geophys. J. R. astr. Soc, 92, 207-222.

Snieder, R., 2002. Scattering of surface waves, in Scattering and Inverse Scattering in Pure and Applied Science, eds. R. Pike and P. Sabatier, Academic Press, San Diego: 562-577.

Spetzler, J., J. Trampert, and R. Snieder, 2001. Are we exceeding the limits of the great circle approximation in global surface wave tomography?, Geoph. Res. Let. 28(12): 2341-2344.

Spetzler, J., J. Trampert, and R. Snieder, 2002. The effect of scattering in surface wave tomography, Geophys. J. Int., 149: 755-767.

Trampert, J., and J. Woodhouse, 1995. Global phase velocity maps of Love and Rayleigh waves between 40 and 150 seconds, Geophys. J. Int., 122: 675-690.

Trampert, J., and J. Woodhouse, 1996. High resolution global phase velocity distributions. Geophys. Res. Lett., 23: 21-24.

Trampert, J., and J. Woodhouse, 2003. Global anisotropic phase velocity maps for fundamental mode waves between 40 and 150 seconds, Geophys. J. Int., 154: 154-165.

Vasco, D.W., J.E. Peterson, and E.L. Majer, 1995. Beyond ray tomography: Wavepath and Fresnel volumes, Geophysics, 60: 1790-1804.

Wang, Z. and F.A. Dahlen, 1995. Validity of surface-wave ray theory on a laterally heterogeneous earth, Geophys. J. Int., 123: 757-773.

Wessel, P., and W.H.F. Smith, 1991. Free software helps map and display data, EOS, 72: 441.

Wessel, P., and W.H.F. Smith, 1995. New version of the Generic Mapping Tools released, EOS, 76: 329.

Woodhouse, J.H., 1974. Surface waves in a laterally varying layered structure, Geoph. J. R. astr. Soc., 37: 461-490.

Woodhouse, J. H. and T. P. Girnius, 1982. Surface waves and free oscillations in a regionalized Earth model, Geoph. J. R. astr. Soc., 68: 653-673.

Yomogida, K., and K. Aki, 1987. Amplitude and phase data inversion for phase velocity anomalies in the Pacific Ocean basin, Geoph. J. R. astr. Soc., 88, 161-204.

Yoshizawa, K. and B.L.N. Kennett, 2002. Determination of the influence zone for surface wave paths, Geophys. J. Int., 149: 439-452.

Table 1. Number of paths before and after rejection of outliers, and after the consistency test.

Period sec	Wave Type	Number of Input Paths	Rms, Ph. Vel. Res., m/s	Number of Selected Paths (1st Stage)	Number of Selected Paths (2nd Stage)	Rms, Ph. Vel. Errors, m/s
50	R1	54168	22	49179	30543	6.7
50	R2	21347	26	14398	12672	4.6
100	R1	54168	26	50215	30446	8.7
100	R2	21347	30	15671	13681	3.2

Table 2. Comparison of tomographic maps for Northern and Southern regions obtained with R1 and R1 + R2 data sets.

Region	Period s	Wavetype	Correlation Coefficient	Rms of difference m/s
$45° - 90°N$	50	Rayleigh	0.970	22
$45° - 90°N$	100	Rayleigh	0.968	23
$45° - 90°S$	50	Rayleigh	0.902	35
$45° - 90°S$	100	Rayleigh	0.821	44

Table 3. Misfit between predicted and observed traveltimes and phase velocities
(all the World).

Period s	Map	Type of Data	Number of Paths	Rms (traveltime) s	Variance[†] Reduction,%	Rms (phase velocity), m/s
50	R1+R2	R1+R2	39964	10.90	29.1	15.9
50	R1+R2	R1	27310	9.35	14.6	17.4
50	R1+R2	R2	12654	15.44	42.7	8.2
50	R1	R1	27310	9.02	20.4	16.8
50	R1	R2	12654	19.56	8.12	10.1
100	R1+R2	R1+R2	40483	10.27	23.1	19.2
100	R1+R2	R1	26852	8.93	11.0	20.4
100	R1+R2	R2	13631	10.87	35.1	6.2
100	R1	R1	26852	8.64	16.8	19.6
100	R1	R2	13631	17.86	-13.6	10.0

† Variance reduction is relative to predicted velocities from Shapiro & Ritzwoller (2002).

Table 4. Misfit between predicted and observed traveltimes and phase velocities
(the Southern Hemisphere).

Period s	Map	Type of Data	Number of Paths	Rms (traveltime) s	Variance[†] Reduction,%	Rms (phase velocity), m/s
50	R1+R2	R1+R2	5006	11.01	24.5	21.1
50	R1+R2	R1	3757	9.01	10.1	22.6
50	R1	R1	3757	8.31	25.1	23.5
100	R1+R2	R1+R2	5156	10.66	17.8	24.5
100	R1+R2	R1	3708	9.31	11.5	27.0
100	R1	R1	3708	8.66	23.5	25.5

† Variance reduction is relative to predicted velocities from Shapiro & Ritzwoller (2002).
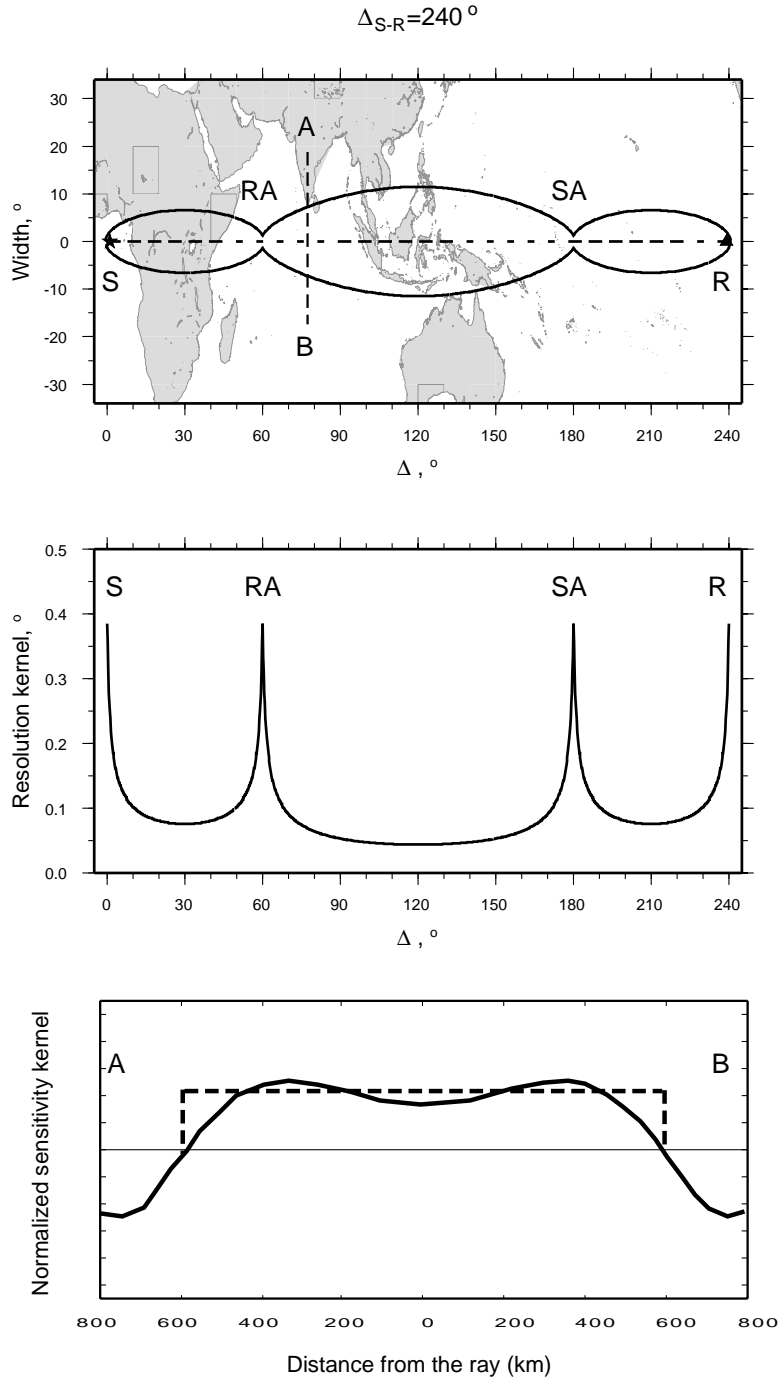
Figure 1: Definition of a sensitivity zone for the PREM model of the Earth (top); its kernel along the great circle SR (middle) and along AB cross-section (bottom) where the solid line corresponds to the Born/Rytov approximation and the dashed line represents the approximation used in this study. Abbreviations used: S - source, R - receiver, RA - receiver's antipode, SA - source's antipode. Epicentral distance $\Delta_{S-R} = 240°$.
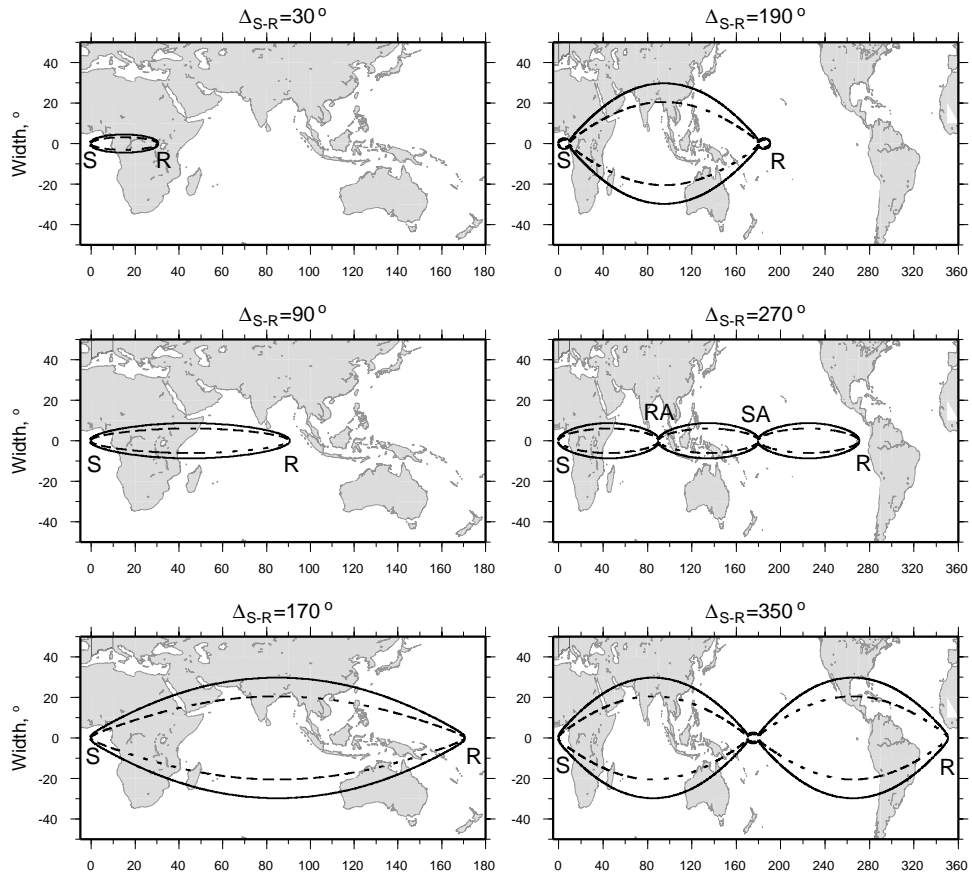
Figure 2: The zones of sensitivity for minor and major arcs for Rayleigh waves at periods $T = 100\,s$ (solid lines) and $T = 50\,s$ (dashed lines) and indicated epicentral distances.
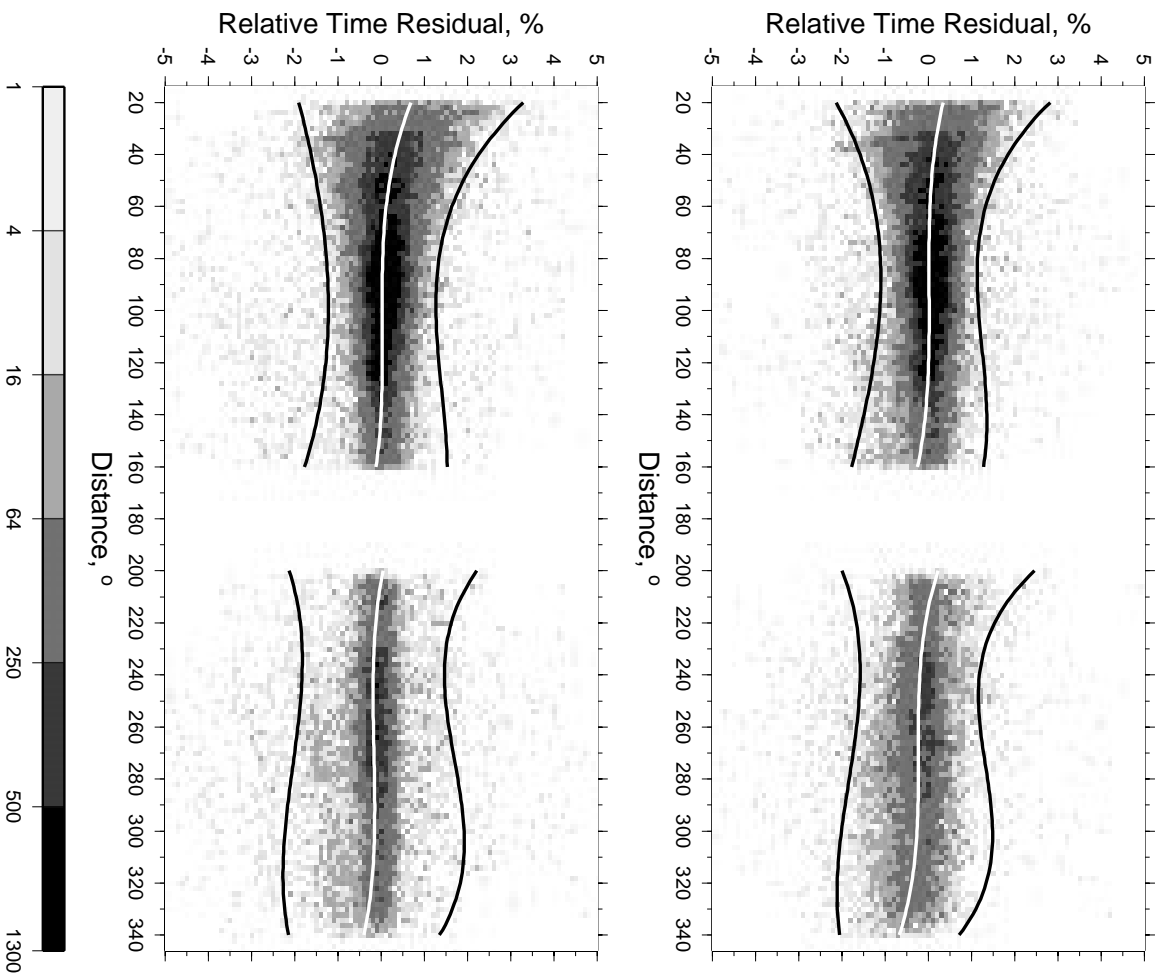
Figure 3: Shaded plots of the density of relative traveltime residuals [(observed - predicted)/predicted] for the entire R1 and R2 phase velocity data set presented versus epicentral distance. Darker shades indicate larger number of residuals. The white lines show the running mean, and the black lines show $\pm 2.5\sigma$. Density is defined as the number of residuals inside each $2° \times 0.1\%$ cell.
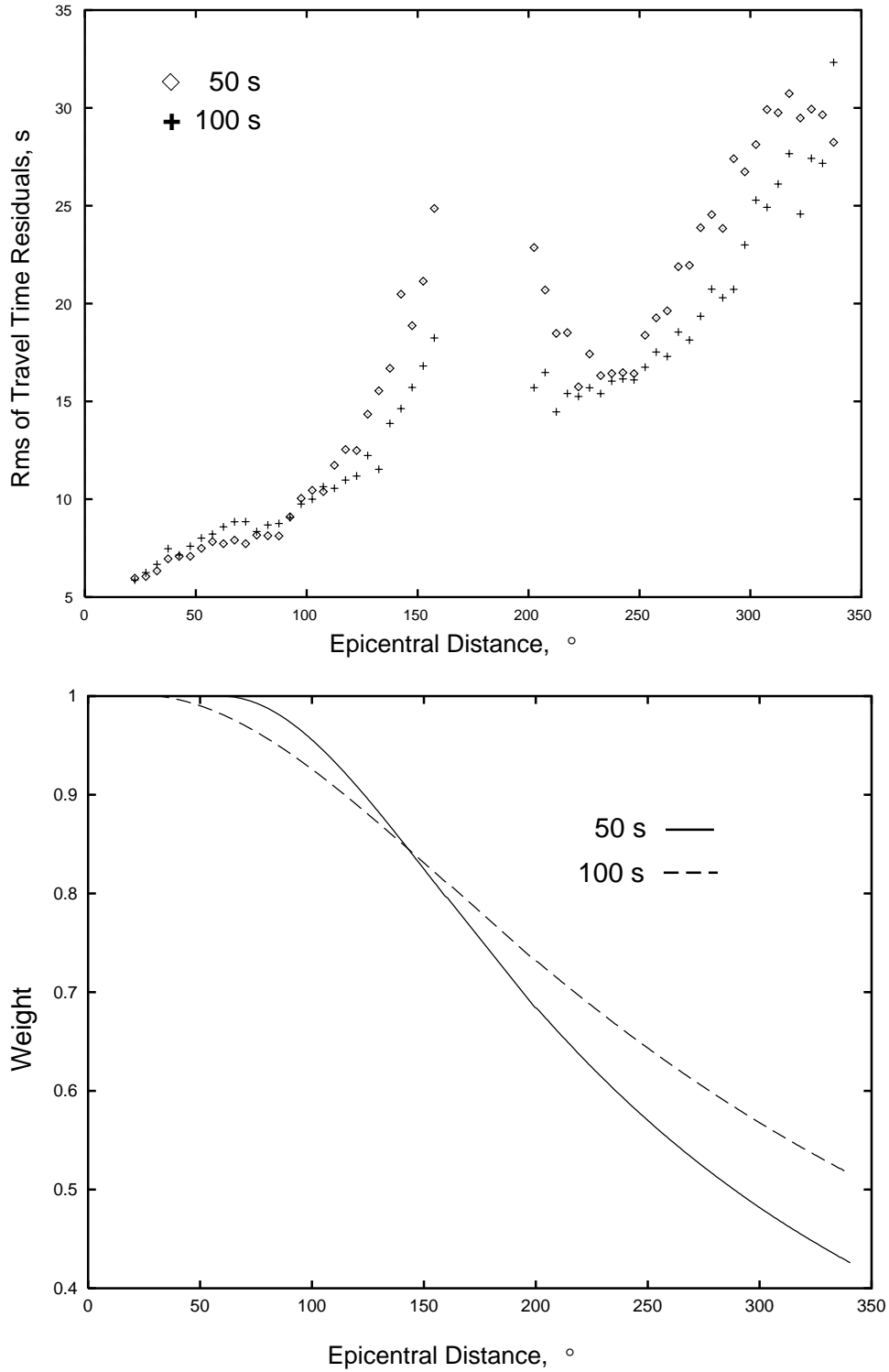
Figure 4: Rms of phase traveltime residuals for the cleaned data set as functions of epicentral distance for 50 and 100 s Rayleigh waves (top). Weights as functions of epicentral distance (bottom).

R1, 50 s   **R2, 50 s**

Eurasia

Pacific

Antarctica
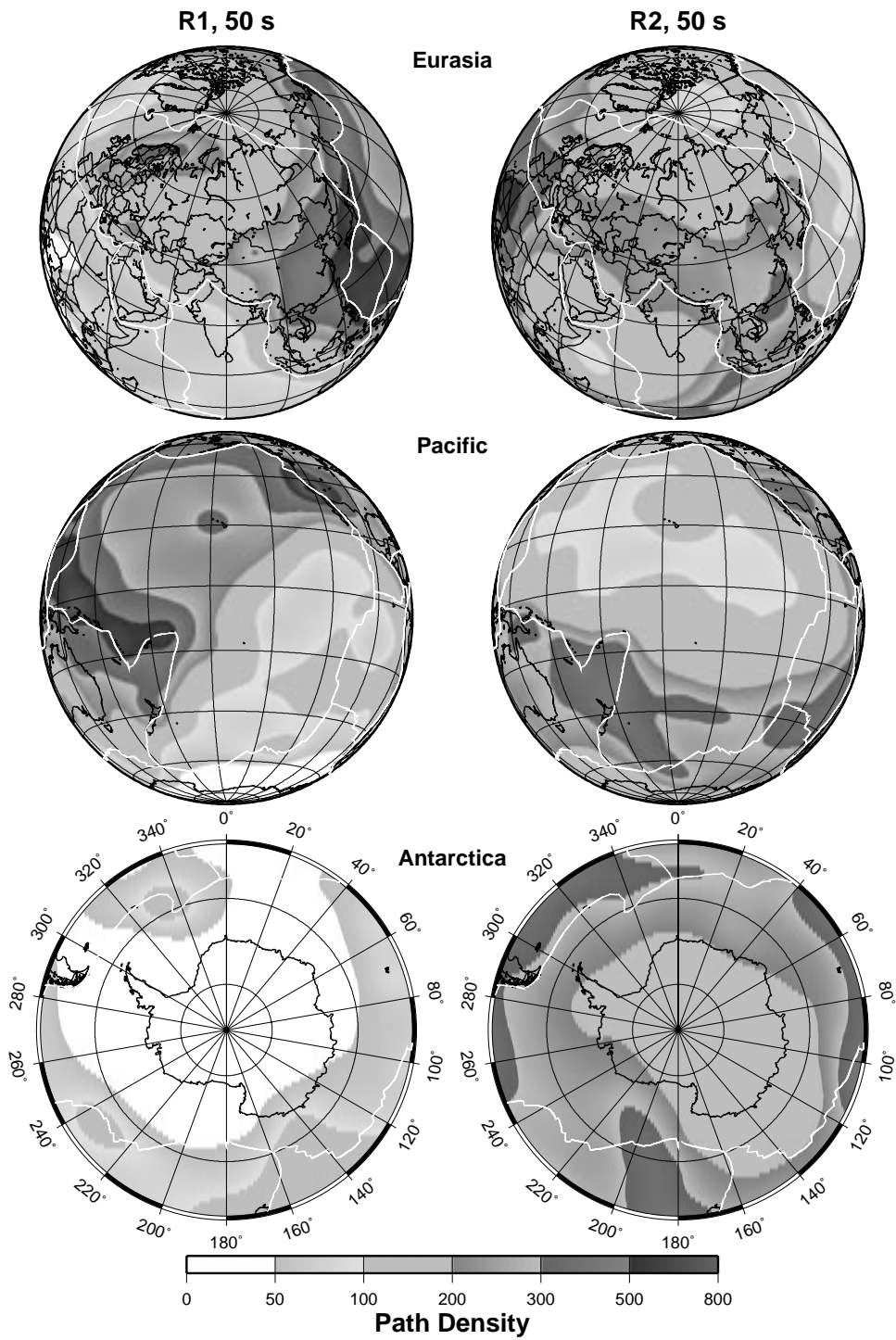
Path Density

Figure 5: Pseudo-path density of 50 s surface waves across Eurasia, the Pacific, and Antarctica: minor arc data (left side); major arc data (right side). This approximates the number of the rays in each $2° \times 2°$ cell.
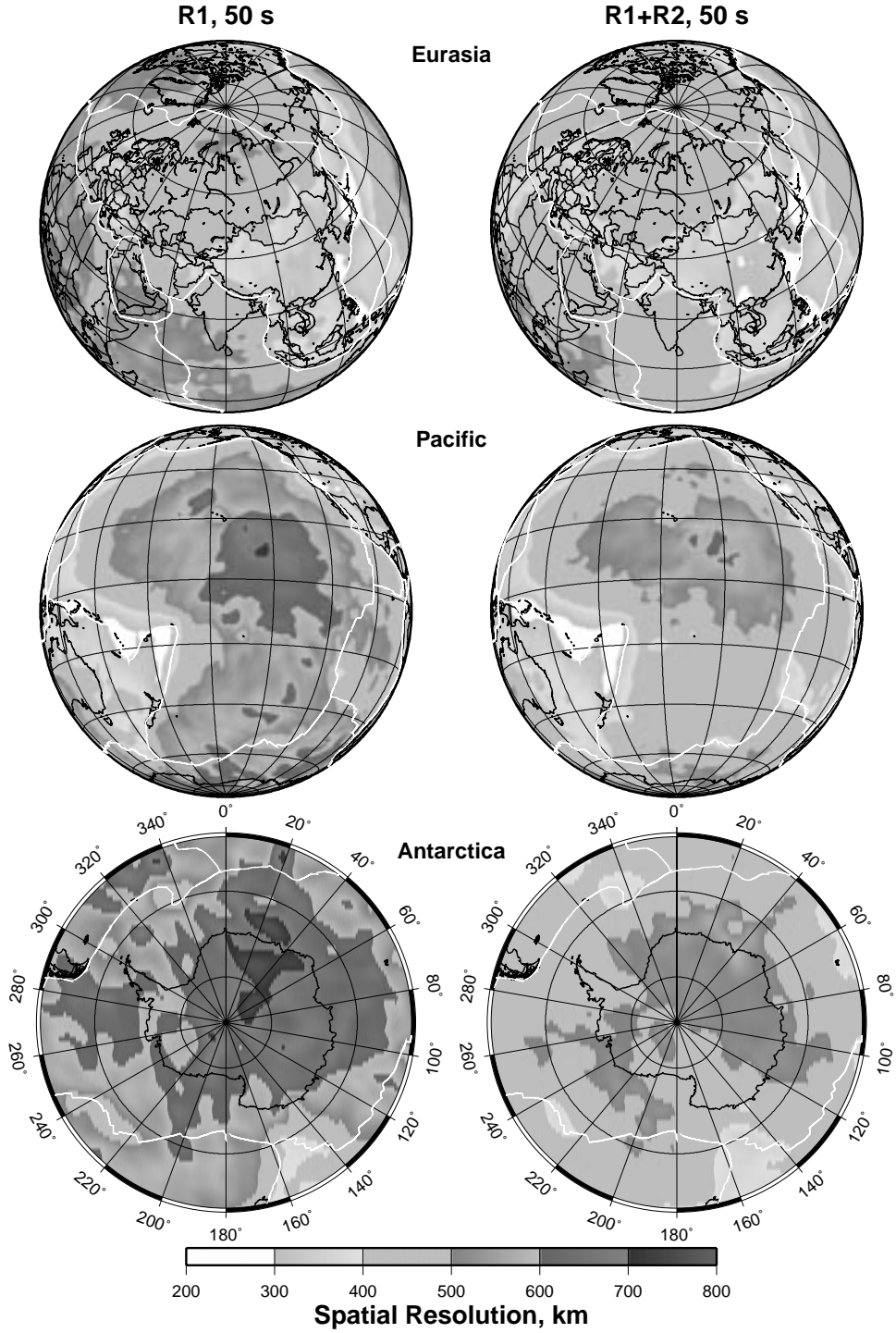
Figure 6: Spatial resolution of 50 s surface wave tomography across Eurasia, the Pacific, and Antarctica: minor arc data (left side); minor and major arc data (right side).
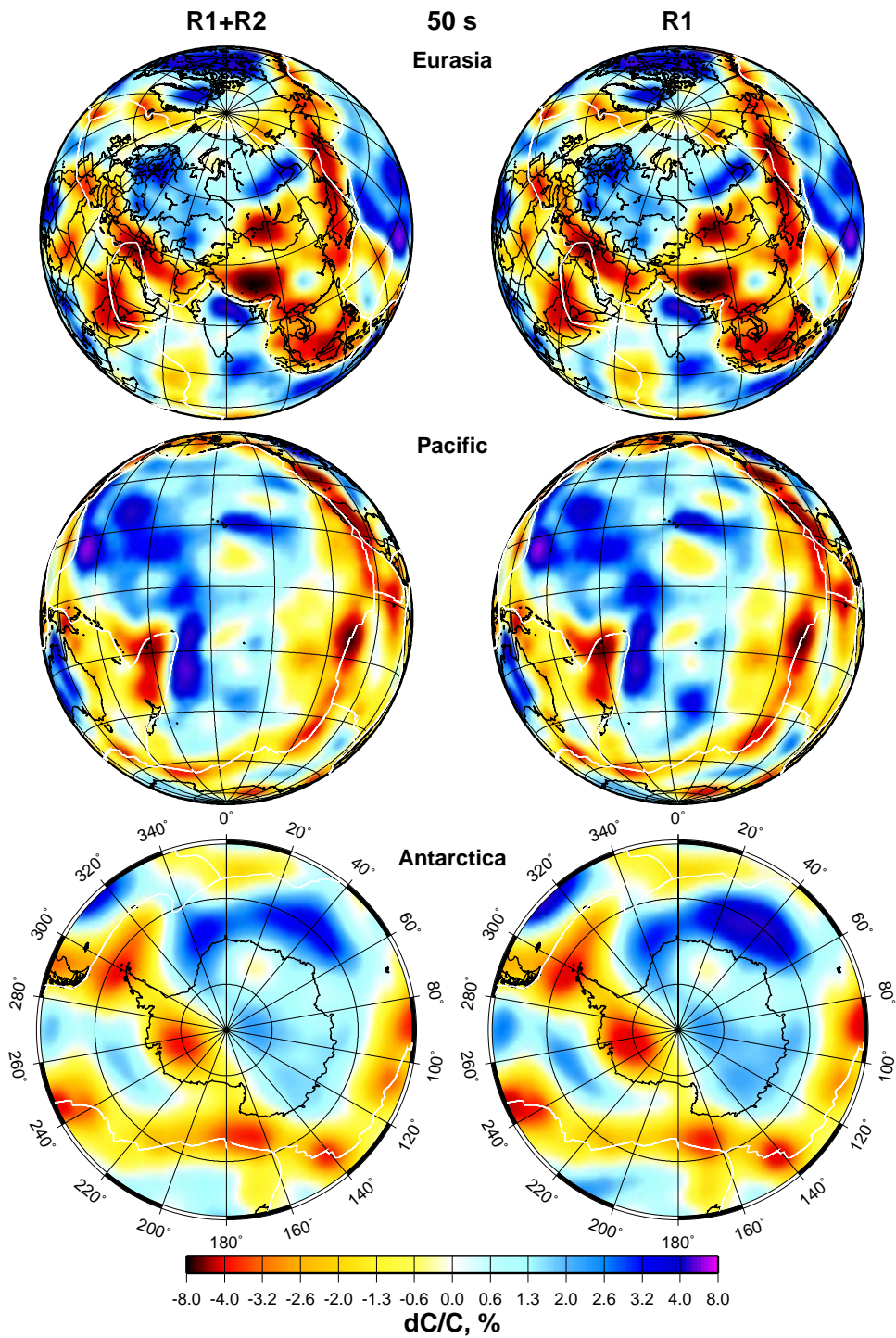
Figure 7: Tomographic maps for 50 s Rayleigh waves across Eurasia (top), the Pacific (middle), and Antarctica (bottom): minor and major arc data combined (left side); only minor arc data used (right side).
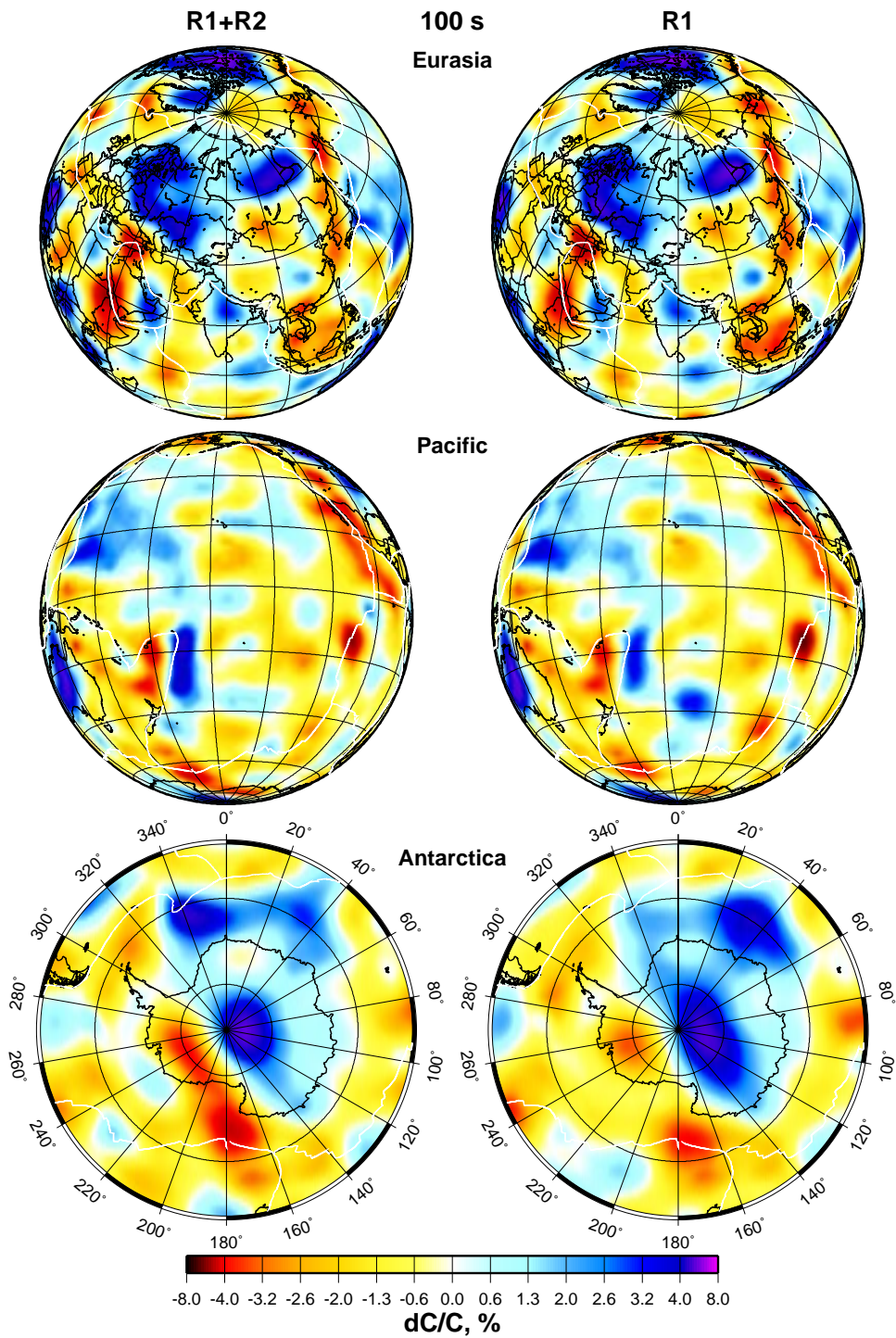
Figure 8: Tomographic maps for 100 s Rayleigh waves across Eurasia (top), the Pacific (middle), and Antarctica (bottom): minor and major arc data combined (left side); only minor arc data used (right side).
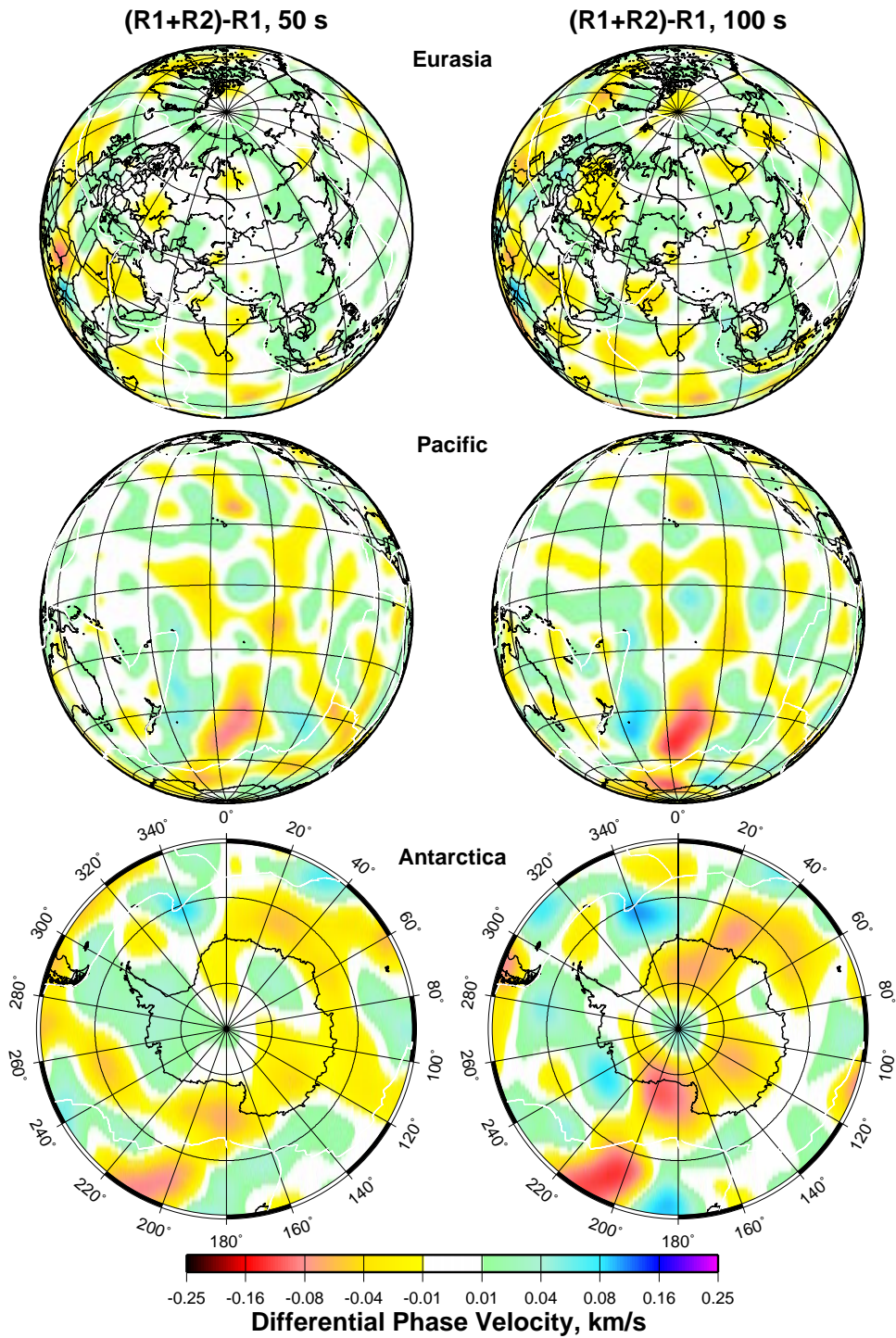
Figure 9: Differential tomographic maps for 50 s (left side) and 100 s (right side) Rayleigh waves across Eurasia (top), the Pacific (middle), and Antarctica (bottom): values of phase velocities at [R1] maps are subtracted from values at the same nodes of [R1+R2] maps.